




Article

Process Induced Preheating in Laser Powder Bed Fusion Monitored by Thermography and Its Influence on the Microstructure of 316L Stainless Steel Parts

Gunther Mohr ^{1,2,*}, Konstantin Sommer ^{1,3}, Tim Knobloch ^{1,2}, Simon J. Altenburg ¹ , Sebastian Recknagel ¹, Dirk Bettge ¹  and Kai Hilgenberg ¹ 

¹ Bundesanstalt für Materialforschung und-prüfung (BAM), Unter den Eichen 87, 12205 Berlin, Germany; konstantin.sommer@bam.de (K.S.); tim.knobloch@bam.de (T.K.); Simon.Altenburg@bam.de (S.J.A.); sebastian.recknagel@bam.de (S.R.); Dirk.Bettge@bam.de (D.B.); kai.hilgenberg@bam.de (K.H.)

² Institute of Machine Tools and Factory Management, Technische Universität Berlin, Straße des 17. Juni 135, 10623 Berlin, Germany

³ Institute of Materials Science and Technology, Chair of Metallic Materials, Technische Universität Berlin, Straße des 17. Juni 135, 10623 Berlin, Germany

* Correspondence: gunther.mohr@bam.de



Citation: Mohr, G.; Sommer, K.; Knobloch, T.; Altenburg, S.J.; Recknagel, S.; Bettge, D.; Hilgenberg, K. Process Induced Preheating in Laser Powder Bed Fusion Monitored by Thermography and Its Influence on the Microstructure of 316L Stainless Steel Parts. *Metals* **2021**, *11*, 1063. <https://doi.org/10.3390/met11071063>

Academic Editor: Sergey N. Grigoriev

Received: 7 June 2021

Accepted: 29 June 2021

Published: 1 July 2021

Publisher's Note: MDPI stays neutral with regard to jurisdictional claims in published maps and institutional affiliations.



Copyright: © 2021 by the authors. Licensee MDPI, Basel, Switzerland. This article is an open access article distributed under the terms and conditions of the Creative Commons Attribution (CC BY) license (<https://creativecommons.org/licenses/by/4.0/>).

Abstract: Undetected and undesired microstructural variations in components produced by laser powder bed fusion are a major challenge, especially for safety-critical components. In this study, an in-depth analysis of the microstructural features of 316L specimens produced by laser powder bed fusion at different levels of volumetric energy density and different levels of inter layer time is reported. The study has been conducted on specimens with an application relevant build height (>100 mm). Furthermore, the evolution of the intrinsic preheating temperature during the build-up of specimens was monitored using a thermographic in-situ monitoring set-up. By applying recently determined emissivity values of 316L powder layers, real temperatures could be quantified. Heat accumulation led to preheating temperatures of up to about 600 °C. Significant differences in the preheating temperatures were discussed with respect to the individual process parameter combinations, including the build height. A strong effect of the inter layer time on the heat accumulation was observed. A shorter inter layer time resulted in an increase of the preheating temperature by more than a factor of 2 in the upper part of the specimens compared to longer inter layer times. This, in turn, resulted in heterogeneity of the microstructure and differences in material properties within individual specimens. The resulting differences in the microstructure were analyzed using electron back scatter diffraction and scanning electron microscopy. Results from chemical analysis as well as electron back scatter diffraction measurements indicated stable conditions in terms of chemical alloy composition and austenite phase content for the used set of parameter combinations. However, an increase of the average grain size by more than a factor of 2.5 could be revealed within individual specimens. Additionally, differences in feature size of the solidification cellular substructure were examined and a trend of increasing cell sizes was observed. This trend was attributed to differences in solidification rate and thermal gradients induced by differences in scanning velocity and preheating temperature. A change of the thermal history due to intrinsic preheating could be identified as the main cause of this heterogeneity. It was induced by critical combinations of the energy input and differences in heat transfer conditions by variations of the inter layer time. The microstructural variations were directly correlated to differences in hardness.

Keywords: additive manufacturing; laser powder bed fusion; selective laser melting; laser beam melting; in-situ process monitoring; thermography; heat accumulation; inter layer time; cellular substructure

1. Introduction

Additive manufacturing (AM) technologies provide promising advantages for the production of highly individual and complex structures, mass customization, the integra-

tion of functional designs, and the reduction of lead times [1,2]. The working principles of various metallic AM processes are described, e.g., by DebRoy et al. [3]. Although laser powder bed fusion (L-PBF) is the most prevalent AM technology for metal part production [4], the homogeneity of the material produced is still problematic. Inhomogeneity of the microstructure, defect density, and resulting mechanical properties within parts or in comparison of different parts have been alluded by several authors [3,5–7]. Microstructural variations in AM components are a major challenge, especially for safety-critical components [6,8,9].

A high degree of freedom in design in L-PBF offers the chance to produce complex shaped geometries. However, the geometry itself can influence the thermal history of a part during manufacturing as it might change the conditions of heat dissipation [10–12]. A detrimental change of the heat conduction through the part towards the base plate, as well as a significant change of the inter layer time (ILT), can lead to severe heat accumulation of the part or areas of local overheating. This, in turn, results in deviations of the thermal history and eventually affects part quality [5,10,13]. In addition to the geometry, there are many other influencing factors on the thermal history of a L-PBF component. These comprise, for instance, processing parameters, scanning strategies, support design, or ratio of area exploitation [3,5,11,12]. The thermal history of an L-PBF process is an important factor for the development of the microstructure, as it is influenced by the transient temperature fields during manufacturing. It is well known that variations of temperature gradients can significantly affect the microstructural development. Lower cooling rates are generally expected to develop a coarser microstructure than higher cooling rates [1,14].

The microstructure of 316L processed by L-PBF typically shows features that can be observed over a broad range of length scales. The features include melt pool boundaries, grains and sub-grains, cellular substructures of grains, segregations, dislocation networks at the boundaries of cell structures, and nanoscale precipitations [15–18]. The shape of melt pool boundaries is influenced by the scanning strategy and process parameters. Their shape and penetration depth strongly depend on the melting mode [19]. Patel and Vlasea [20] reported on the occurrence of deep penetration mode welding (keyhole mode welding) and transition mode welding over a broad range of process parameters in L-PBF processing of 316L. According to Krakhmalev et al. [16], the grains consist of cellular substructures due to high cooling rates, whereby the cells grow epitaxially, starting at melt pool boundaries. The cellular substructures grow competitively based on their crystallographic orientation and the local thermal gradients inside the melt pool [16]. The growth of cellular substructures in 316L processed by L-PBF typically leads to segregation of Mn, Mo, and Cr and dislocation networks at cell boundaries [15,16]. The features of these cellular substructures, namely, the cell size and the occurrence of micro-segregations, strongly depend on the local directional solidification conditions [9]. Pinomaa et al. [9] recently quantified the influence of the local thermal gradient and local melt pool solidification rate on these features as well as on the mode of growth by conducting phase field simulations.

David et al. [21] investigated the effect of rapid solidification on the weld metal microstructures in different stainless steel compositions in the late 1980s. They integrated the influence of the cooling rate into the Schaeffler diagram [21]. It can be derived from their work that 316 stainless steel solidifies as fully austenitic at cooling rates above $0.28 \times 10^6 \text{ K}\cdot\text{s}^{-1}$. Due to the lower austenite stabilizing carbon content in 316L stainless steel, these cooling rates might shift to slightly higher values for 316L. Bajaj et al. [22] conducted an intense review on steels in L-PBF and direct energy deposition. They reported fully austenitic phase for 316L when processed by L-PBF. Krakhmalev et al. [16] also mentioned a fully austenitic phase with some very exceptional cases of the occurrence of a ferritic phase.

Additionally, the occurrence of spherical nano-sized oxide inclusions has been reported for 316L produced by L-PBF [16]. Lou et al. [23] investigated the influence of these Si- and Mn-rich oxide inclusions. They concluded that these oxide inclusions can be responsible for the initiation of micro-voids with detrimental effects on impact toughness.

They compared the measured impact toughness with values from literature for specimens produced by powder metallurgy route and wrought material, revealing distinct beneficial effects when the oxygen content was below 0.02%.

In addition to these crystallographic features of the microstructure, internal defects such as delamination, cracks, and pores can occur [24]. Pores can be categorized into so-called lack-of-fusion defects and gas porosity [25]. Lack of fusion defects are irregularly-shaped pseudo pores, which essentially are cavities resulting from insufficient melting and insufficient material cohesion due to deficient melt pool dimensions or inadequate choice of processing parameters such as the hatch distance between single melt tracks [25,26]. A main source of spherical gas porosity can be found in detached and entrapped vapor bubbles of the vapor capillary in an instable keyhole welding mode [25,27].

The possibility to influence the temperature gradients occurring in the process has been shown in different studies. On the one hand, there are approaches to tailor a microstructure during the L-PBF process by adjusted sets of processing parameters [28,29] or modifications of the laser beam shape and intensity profile [30,31]. On the other hand, there are approaches to decrease residual stresses or crack susceptibility by, e.g., remelting or platform preheating adjustments [32,33]. These approaches have in common the aim to purposely influence the initial resulting microstructure of an L-PBF specimen or component either throughout the entire geometry or within particular regions. However, there are further situations where variations of microstructures in L-PBF processes should be considered. This includes unplanned microstructural variations that are induced due to heat accumulation during the process.

The accumulation of heat during the build-up of an L-PBF part essentially alters the preheating condition at the surface to be coated by the new powder layer which is subsequently exposed by laser radiation. Therefore, the initial thermal conditions prior to the exposure by laser radiation are altered. As a result, the thermal gradients during melting and solidification might change with varying initial preheating temperature. A significant change of the preheating temperature of the part can alter the melt pool dimensions and their solidification conditions [5,34]. As pointed out by Krakhmalev et al. [16], the cellular mode of solidification in 316L processed by L-PBF occurs at high solidification rates and steep thermal gradients. The resulting microstructural feature sizes such as cell spacing depend on these conditions [16]. They might change when the preheating temperature increases due to heat accumulation. Depending on the magnitude of the variation in preheating condition, the induced variations on the microstructure can be strong enough to affect the mechanical properties of a component [5]. In addition to potential changes of the melt pool shape and the melt pool dimensions, as well as potential changes of crystallographic features, an increase of the preheating temperature may also be able to shift the melting mode to an unstable region with propensity to develop detrimental keyhole porosity [5].

The authors [5] investigated process conditions where heat accumulation was provoked to occur during the L-PBF fabrication of simple cuboid specimens of 316L stainless steel at application relevant build heights, i.e., the specimens height was bigger than 100 mm. Using a mid-wavelength infrared thermography camera as an in-situ thermal monitoring device, significant differences in cooling behavior were revealed. Specimens were produced applying three distinct ILT and three distinct volumetric energy densities (VED). The build height was also identified as an affecting factor. The authors correlated the differences in cooling conditions with differences in apparent sub-grain sizes measured by light microscopy, melt pool depths, and hardness values. To refine the knowledge of process-property-relationship and to prove the relationships measured by light microscopy, a more detailed analysis of the influence of in-situ heat accumulation on the microstructure of 316L components is required. Therefore, this study pursues the examinations of the same specimens used in [5] and investigates the microstructure by means of electron back scattered diffraction (EBSD) in greater detail. In addition, scanning electron microscopy (SEM) is used to compare the feature size of the cellular substructure. The alloy composition

of the produced specimens as well as a potential oxygen intake is measured by different methods of chemical analysis. By applying recently conducted temperature adjustments of the infrared (IR) monitoring set-up [35], real temperatures of the powder surfaces could be quantified. The layer-wise increase of the preheating temperatures of the specimens was measured in-situ over the entire build process of the specimens. The results are discussed with respect to recent publications. Results of hardness measurements were taken from [5].

Although there have been extensive investigations on L-PBF of 316L, a quantification of process-induced preheating of the specimens during manufacturing and its correlation to changes in crystallographic features is currently missing. Information about the magnitude of microstructural changes induced by critical but still realistic process conditions is important. It will help to improve the evaluation of a real part of the production and the comparability of test coupons that are manufactured under certain processing conditions. Effects of processing parameters such as scanning velocity or laser power have been studied extensively. However, the build height and the ILT are often not considered. Their influence may not be considered significant in the case of typical 10 mm cubic specimens or in the case of high ratios of area exploitation within the powder bed. They may become an affecting factor in the case of complex real part geometries with varying area exploitations over the build height. Additionally, the current trends in the development of new L-PBF machines (e.g., multi laser machines) are expected to decrease the ILT, which increases the need for reliable data about potential microstructural heterogeneity.

2. Materials and Methods

2.1. Material and Specimen Manufacturing by L-PBF

In this section, the key facts about the L-PBF processing conditions and specimens are mentioned. Details were published in [5] where the same set of specimens was examined. Upstanding cuboid-shaped specimens of the dimensions (13 × 20 × 114.5) mm³ were manufactured on a commercial L-PBF single laser system of type SLM280HL (SLM Solutions Group AG, Lübeck, Germany) using a commercial 316L stainless steel powder. Table 1 shows the chemical composition of the powder material according to supplier's information. Figure 1 depicts the geometry of the specimens and contains a schematic of the applied bidirectional scanning strategy with 90° rotation between layers. It also highlights the parts of the specimen that were taken for the deeper analysis in this study in grey color. These were basically the volumes of the lower 12.5 mm (including excess material for part removal) and of the upper 10 mm of each specimen.

Table 1. Chemical composition of the 316L raw powder material according to supplier's information and the respective min. and max. values as per the material specification by DIN EN 10088-3 [36]. The figures express mass fractions in %.

| Specification | C | Si | Mn | P | S | Cr | Mo | Ni | N | Fe |
|---------------|-------|-----|------|-------|-------|------|------|------|-----|------|
| Min. | - | - | - | - | - | 16.5 | 2.0 | 10.0 | - | bal. |
| Max. | 0.03 | 1.0 | 2.0 | 0.045 | 0.03 | 18.5 | 2.5 | 13.0 | 0.1 | bal. |
| Powder | 0.017 | 0.6 | 0.92 | 0.012 | 0.004 | 17.7 | 2.35 | 12.6 | 0.1 | bal. |

The specimens were manufactured at three distinct ILT and at each ILT at three distinct levels of VED by varying the scanning velocity v_s , i.e., nine different types of specimens were built. Each specimen type was built up twice, as stated in [5]. The other manufacturing parameters were kept constant. All process parameters are summarized in Table 2.

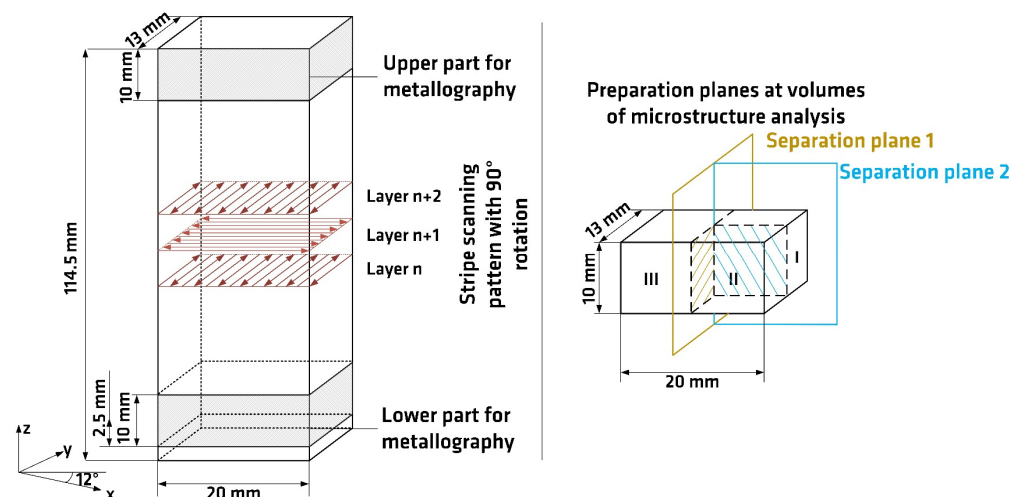


Figure 1. Specimens' geometry. Grey volumes were designated for microstructure analysis and were cut according to the preparation planes in the schematic. Adapted from ref. [5].

Table 2. Processing parameters.

| Processing Parameters | Level |
|---------------------------------|---|
| Layer thickness | 0.05 mm |
| Laser power | 275 W |
| Hatch distance | 0.12 mm |
| Platform preheating temperature | 100 °C |
| Inter layer time | Short: 18 s |
| | Intermediate: 65 s |
| | Long: 116 s |
| Volumetric energy density | Low: 49.12 J·mm ⁻³ $v_s = 933 \text{ mm} \cdot \text{s}^{-1}$ (75% of basis VED) |
| | Basis: 65.48 J·mm ⁻³ $v_s = 700 \text{ mm} \cdot \text{s}^{-1}$ |
| | High: 81.85 J·mm ⁻³ $v_s = 560 \text{ mm} \cdot \text{s}^{-1}$ (125% of basis VED) |

The ILT of layer number n was defined in [5] and is explained by Equation (1).

$$\text{ILT}_{\text{layer } n} = \text{time for powder recoating} + \text{time for laser exposing in layer } n \quad (1)$$

The ILT values for specimen production were chosen according to calculated values from a real part production as compared in [5]. The basis VED parameters represent parameters for the machine and material recommend by the machine's manufacturer but with a simplified scanning strategy. Low VED and high VED parameters were chosen to broaden the energy input, adjusting the VED by plus 25% and minus 25%.

Table 3 gives an overview of the combinations of variable parameters used for specimen production. It also contains the applied methods of analysis, which are described in the following subsections.

Table 3. Matrix of parameter combinations and methods of analysis.

| Level of Inter Layer Time | Level of Volumetric Energy Density | Method of Analysis | | | | |
|---------------------------|------------------------------------|-----------------------------------|-----------------------------|----------------------------------|-------------------|----------------------------|
| | | In-Situ Thermographic Measurement | EBSD Grain Size Measurement | Cell Structure Analysis with SEM | Chemical Analysis | Analysis of Oxygen Content |
| Short ILT | High VED | x | x | x | x | x |
| | Basis VED | x | x | x | x | - |
| | Low VED | x | x | x | - | - |
| Intermediate ILT | High VED | x | x | - | - | - |
| | Basis VED | x | x | x | x | x |
| | Low VED | x | x | - | - | - |
| Long ILT | High VED | x | x | - | - | - |
| | Basis VED | x | x | x | - | - |
| | Low VED | x | x | - | x | - |

The specimens were heat-treated under argon gas atmosphere before removal from the base plate. The heat treatment was conducted at 450 °C for 4 h after the process to relieve residual stresses without changing the as-built microstructure.

2.2. In-Situ Thermographic Monitoring and Temperature Analysis

The production of the specimens was in-situ monitored using an off-axis infrared camera of type ImageIR8300 (InfraTech GmbH, Dresden, Germany), which was installed on top of the L-PBF system as schematically shown in Figure 2. The camera was calibrated by its vendor for black body radiation. A temperature adjustment was conducted by a determination of emissivity values of 316L powder layers and 316L L-PBF surfaces for the same set-up in previous work [35]. The camera was sensitive in the spectral range from 2 µm to 5.7 µm. The cooled InSb-focal-plane-array of the camera was of size 640 pixel × 512 pixel. The frame rate of the camera was 300 Hz for full frame. The measurements were conducted using a subframe image of 160 pixel × 200 pixel. The resulting spatial resolution in the field of view corresponded to approximately 420 µm/pixel. The subframe measurements were conducted at a frame rate of 600 Hz, and a bit resolution of 14 bits was used. The layer-wise recording was triggered by the first overall infrared signal rise above a predefined threshold value. Then, a predefined number of 40 bygone time steps were taken as start of the recording by using a circular buffer. The duration of the recording was set by the definition of a certain number of frames to acquire. Further details on the thermographic set-up can be found in [5,10], which show qualitative comparisons of the same thermographically gained process information using this set-up.

During the IR measurements of the processes, various internal black body calibration ranges of the camera were used to capture the IR data, since the relevant apparent temperature range succeeded the dynamic temperature range of a single calibration range. The change of the calibration ranges had to be done manually using the camera control software. The following black body calibration ranges were used at a converter resolution of 14 bit: 60 °C–200 °C at an integration time of 89 µs, 125 °C–300 °C at an integration time of 27 µs, 200 °C–400 °C at an integration time of 193 µs, and 300 °C–600 °C at an integration time of 45 µs. They are referred to the following abbreviation scheme: IR-CB 60–200 for the calibration range of 60 °C–200 °C. The conversion of the received IR signal values (apparent temperatures) into temperatures was conducted using a MATLAB (The Mathworks Inc., Natick, MA, USA) routine considering the experimentally determined apparent emissivity values of 316L powder from previous work [35]. For simplification, a constant apparent emissivity value was used over each respective calibration range, i.e., $\varepsilon = 0.33$ for IR-CB 60–200 and for IR-CB 125–300, $\varepsilon = 0.43$ for IR-CB 200–400 and for IR-CB 300–600. Additional information about the temperature adjustment and emissivity

determination using this set-up as well as some theoretical background on that matter can be found in [35].

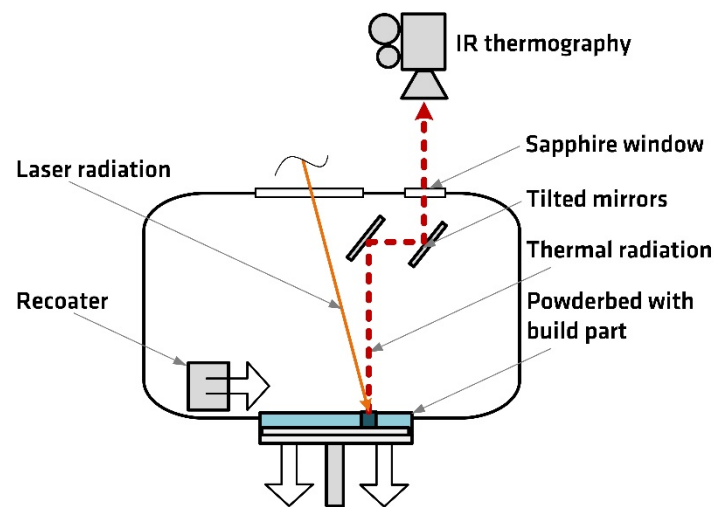


Figure 2. Schematic of the off-axis thermographic monitoring. Reprinted from ref. [10].

In this study, the surface temperatures of the specimens before laser exposure were investigated using the IR camera. Therefore, uncorrected IR signals of an area of $11 \text{ pixels} \times 11 \text{ pixels}$ in the manually selected center of each specimen were averaged and processed using a GNU Octave (open source software) routine. A peak detection was implemented to get comparable sampling times and related values of the preheating IR signals of each specimen for each layer. To this end, the slope of the averaged IR signals was derived and smoothed by using a moving average method. If the slope of the smoothed IR signal is rising above a predefined threshold, it describes the start of the scan process in that area and thereby the interval of interest. The affiliated IR signal value and the timestamp are extracted from the minimum of this interval. These values describe comparable states of each specimen's surface coated with a new powder layer right before the start of the laser exposure of the respective area. Additionally, if there is a temporary drop in the IR signal values the peak detection can be heavily disturbed. This applies, for instance, when the recoater is moving through the field of view during the IR signal recording. The recoating process is accidentally recorded in some cases when, e.g., the layer-wise recording time is too long after the IR camera has been triggered. In this case, the averaged IR signals are filtered beforehand by an optional recoating filter with manually predefined parameter settings. As a last step, the extracted IR value of the comparable state of the specimen is converted to a temperature, using the emissivity values mentioned above. This value is then defined as current preheating temperature of the respective specimen. The measurement uncertainty of the emissivity determination has to be considered [35].

2.3. Analysis of Microstructure Using Electron Back Scatter Diffraction (EBSD)

Electron back scatter diffraction (EBSD) measurements were performed, to investigate the grain structure and phases of the produced specimens. For the measurements, the part II cross sections (see separation plane 1 in Figure 1) were ground with 180, 320, 600, and 1200 grits emery papers and polished using clothes with $3 \mu\text{m}$ and $1 \mu\text{m}$ particle suspensions, followed by MasterMet-2 (Buehler, ITW Test & Measurement GmbH, Esslingen am Neckar, Germany) amorphous $0.02 \mu\text{m}$ colloidal silica suspension. The microscopic measurements were executed on a scanning electron microscope (SEM) Tescan VEGA 3 (TESCAN ORSAY HOLDING a.s., Brno-Kohoutovice, Czech Republic) equipped with an EBSD detector Nordlys (Oxford Instruments plc, Abingdon, England). For acquisition, indexing, and post-processing, the software Aztec 4.1 (Oxford instruments plc, Abingdon, England) was used. An area of $2.25 \text{ mm} \times 3 \text{ mm}$ was measured for every cross section,

using an acceleration voltage of 20 keV, a beam current of approximately 10 nA, a step size of 5 μm , and a pattern size of 168×128 pixels. The low-angle grain boundary (LAGB) criterion was set to 5° to discriminate distinct sub-grains. In addition, for grain discrimination, the high-angle grain boundary (HAGB) criterion was set to 15° .

2.4. Analysis of Cellular Substructures by Scanning Electron Microscopy (SEM)

The investigation of cellular substructures within the grains was performed on the same cross sections after the EBSD measurements. The polished surfaces were etched with Bloech and Wedl II agent (50 mL H_2O , 50 mL HCl, and 0.6 g $\text{K}_2\text{S}_2\text{O}_5$) [37] to contrast the cellular substructure. The measurements were performed on a scanning electron microscope (SEM) Leo Gemini 1530VP (Leo Electron Microscopy Inc., New York, NY, USA) detecting back scattered electrons. Electrons of 20 keV energy were used.

SEM captures of these substructures were made at different locations of the cross-sections, to qualitatively estimate the size distribution of the cells. Cells that grew parallel or close to parallel to the preparation plane were used for the measurement. The cell walls can be imaged due to the topographic effect (bright lines in Figure 3) after etching. The measurement was focused on the number of cell walls within a defined distance in the style of the well-known metallographic grain size measurements by a line intercept method as described in, e.g., DIN EN ISO 643 [38]. To this end, five lines per SEM image with 10 μm length were placed perpendicular to the cell walls which were cut parallel or close to parallel to the preparation plane. Then, the number of intersections with the cellular walls were counted. The number of intersections can be used for relative comparison of the cell size. The lower the number of intersections, the wider are the cells. Three different regions were investigated for each section. In addition, a quantitative estimation can also be derived by dividing the length of the lines by the counted number. Figure 3 depicts an example of the measuring procedure, also presenting the number of intersections with each individual line.

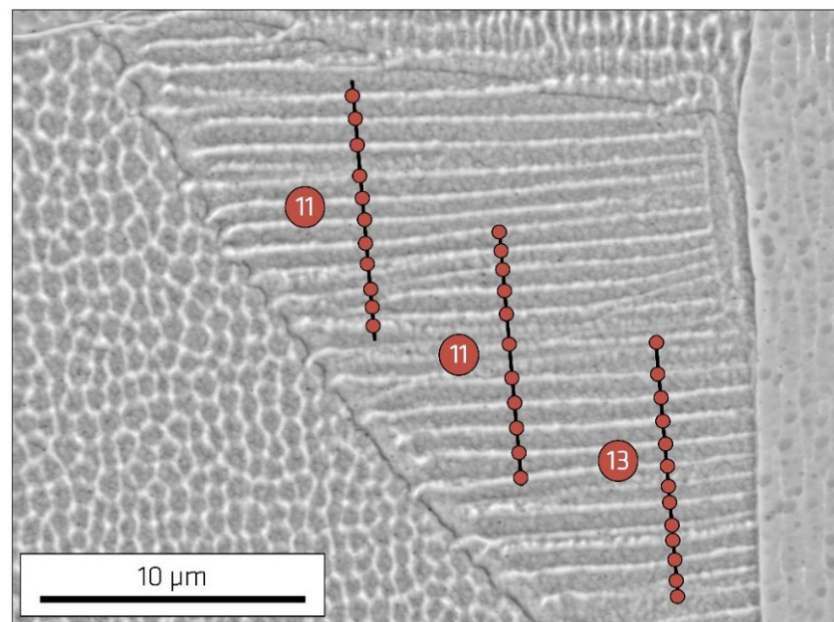


Figure 3. Example of SEM captures of cellular substructures used for estimation of their size distribution by a line intercept method. The numbers in the circles depict the number of intersections of the respective line.

Deng et al. [39] also used such a line intercept method to determine cell sizes of 316L. In contrast to the approach of this study, they applied the line intercept method to cells cut perpendicular to their growth direction. These cells, therefore, appeared in a honeycomb like structure, as visible in the left lower region of the SEM image in Figure 3.

However, the sensitivity to measurement errors seems to be higher in this case as compared to a line intercept measurement through the parallel cell walls. This is due to a minor effect of a potential tilt angle of the cross section induced by the mechanical preparation would have in the latter case. Pinomaa et al. [9] also measured cell sizes derived from simulations by line interception through parallel cell wall regions, as this was conducted in the present study.

2.5. Analysis of Chemical Composition

The mass fractions of the elements given in Table 1 and of oxygen were determined for selected specimens (see Table 3) using the measurement techniques listed in Table 4. The alloying elements Cr, Ni, Mn, and Mo were determined using X-ray fluorescence spectrometry. Two certified reference materials were used for calibration (ECRM 284-2 and ECRM 284-3, BAM, Berlin, Germany). Since this method is not sufficiently sensitive for each alloying element, traces of Si and P were determined using inductively coupled plasma optical emission spectrometry after decomposition of the material using microwave digestion. For the determination of the non-metals C, S, O, and N, element-analyzers were used, calibrated with different certified reference materials. The analysis was conducted using material of section III in the lower part and upper part of the specimen (see Figure 1). Oxygen measurements were conducted at two separate specimens manufactured under the same processing conditions also using material of section III of the respective parts.

Table 4. Measurement techniques used for precise determination of chemical composition for selected specimens.

| Measurement Technique | Measuring Device | Chemical Element |
|--|---|------------------|
| Combustion/IR-detection | Elementrac CS-i (Eltra GmbH, Haan, Germany) | C |
| | | S |
| Carrier gas hot extraction | G8 Galileo (Bruker Corporation, Billerica, MA, USA) | N |
| | | O |
| X-ray fluorescence spectrometry | NITON XL3t (Thermo Fisher Scientific Inc., Waltham, MA, USA) | Mn |
| | | Cr |
| | | Mo |
| | | Ni |
| Inductively coupled plasma optical emission spectrometry | Spectro Arcos (SPECTRO Analytical Instruments GmbH, Kleve, Germany) | Si |
| | | P |

3. Results

3.1. Surface Temperatures

The in-situ preheating temperature evolution over the build-up process of the specimens is depicted in three different diagrams (Figures 4–6), each showing the preheating temperature over the layer number at a fixed ILT level and different VED levels. In addition, Figure 7 displays the same plots for the basis VED at different ILT levels within one diagram for easier comparison. The captured IR signals were not exploitable for every parameter combination over the entire part due to the narrow band of the set calibration ranges of the IR camera as described in [35]. Only exploitable signals were converted into real temperatures and plotted in the diagrams. Hence, there are some missing parts within some of the curves. Especially, the lower temperature regions were often not resolved within the set calibration ranges. Therefore, considerable shares of the specimens produced with intermediate ILT and long ILT could not be resolved properly in their lower sections.

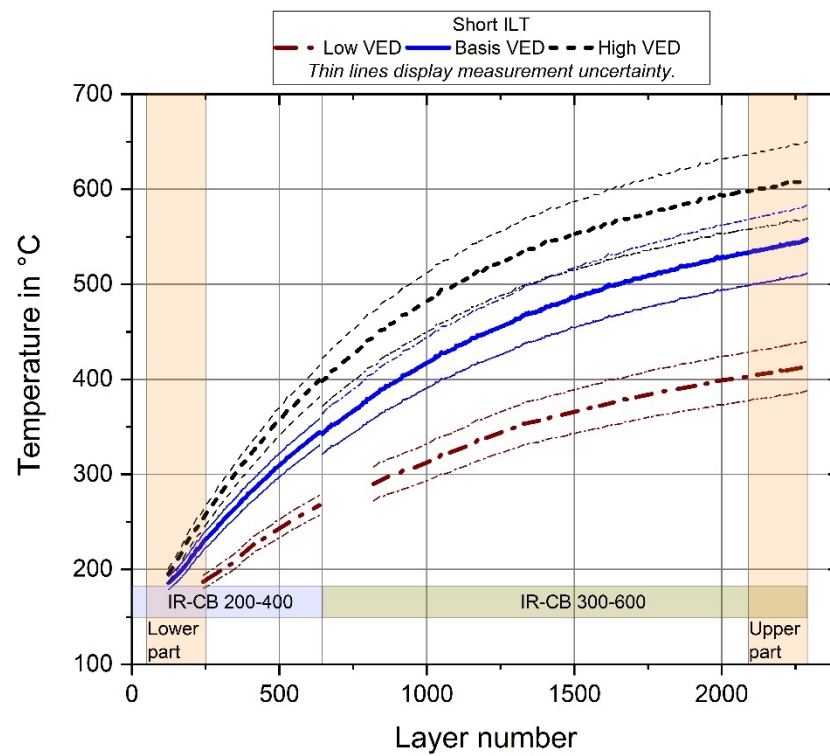


Figure 4. Temperature-layer-number-plots for short ILT. The orange sections highlight the layers of the specimen volumes used for deeper analysis as depicted in Figure 1. The colored bars show the IR calibration ranges (IR-CB) used in the respective layers. Missing parts of the curves (e.g., in the low VED specimen) are due to the narrow bands of the calibration ranges of the IR camera.

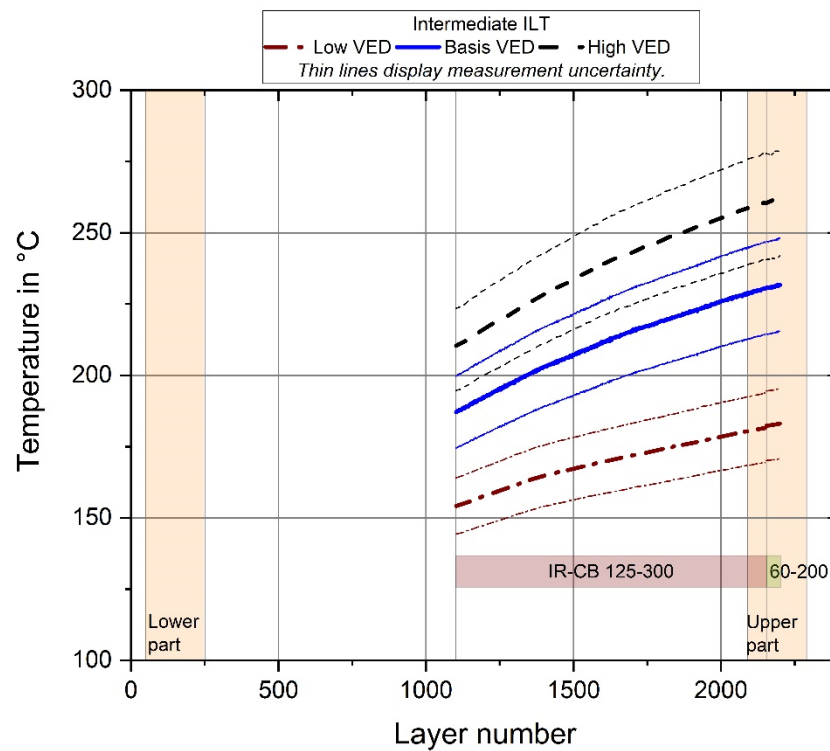


Figure 5. Temperature-layer-number-plots for intermediate ILT. The orange sections highlight the layers of the specimen volumes used for deeper analysis as depicted in Figure 1. The colored bars show the IR calibration ranges (IR-CB) used in the respective layers.

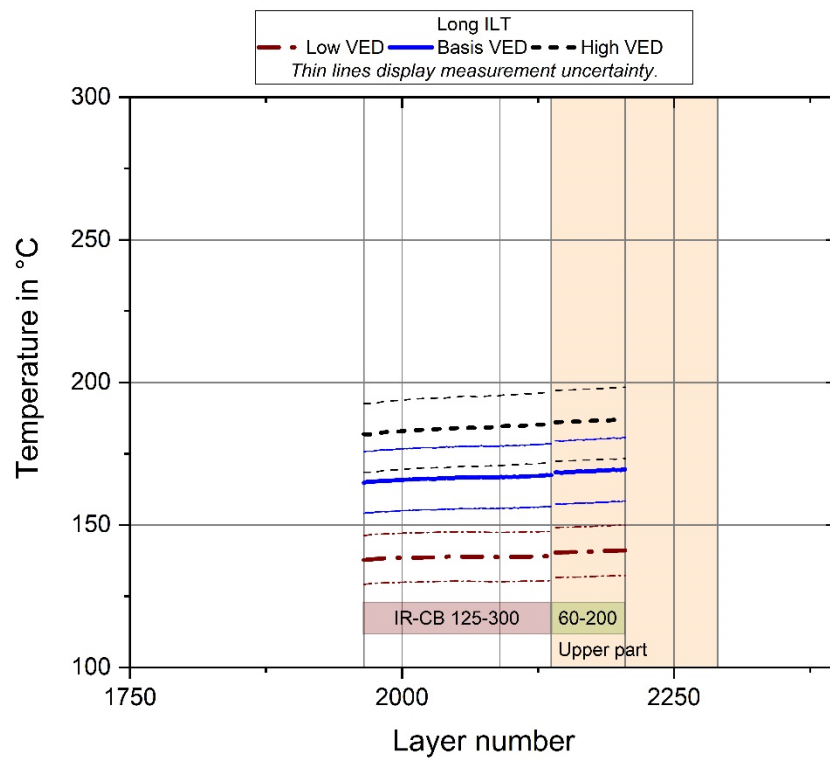


Figure 6. Temperature-layer-number-plots for long ILT. The orange sections highlight the layers of the specimen volumes used for deeper analysis as depicted in Figure 1. The colored bars show the IR calibration ranges (IR-CB) used in the respective layers.

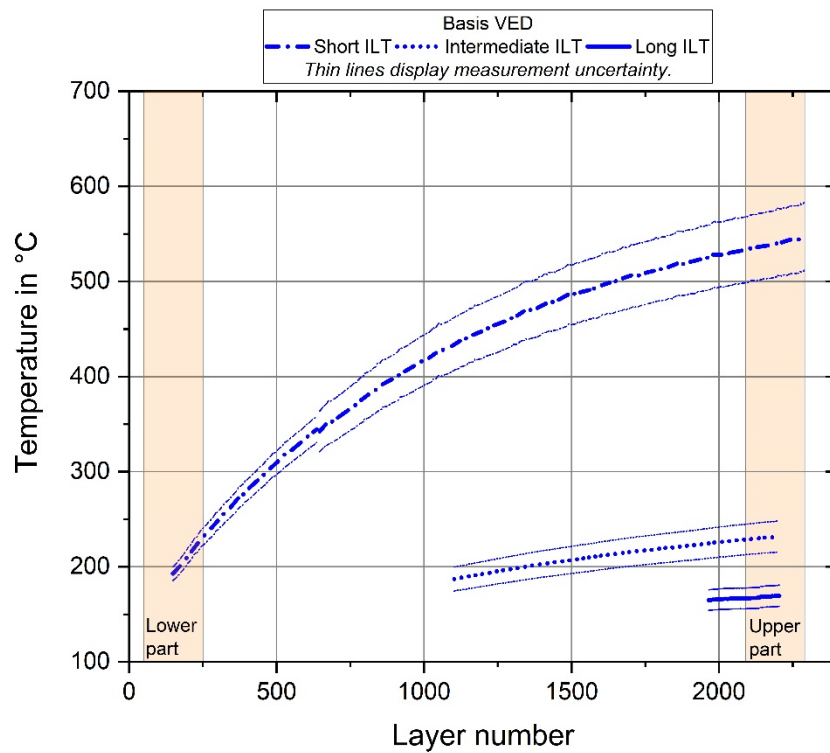


Figure 7. Temperature-layer-number-plots for basis VED. The orange sections highlight the layers of the specimen volumes used for deeper analysis as depicted in Figure 1. Missing parts of the curves are due to the narrow bands of the calibration ranges of the IR camera.

3.2. Grain Size Analysis

The EBSD measurements revealed differences in HAGB grain sizes and LAGB sub-grain sizes between the sections of the window of investigations. The mean LAGB sub-grain sizes and the mean HAGB grain sizes are depicted in Figures 8 and 9 for each combination of ILT and VED (see Table 3) and of the upper part and lower part volumes of investigation (see Figure 1). The corresponding inverse pole figure maps for the specimens' sections marked with capital letters in Figure 8 are shown in Figure 10.

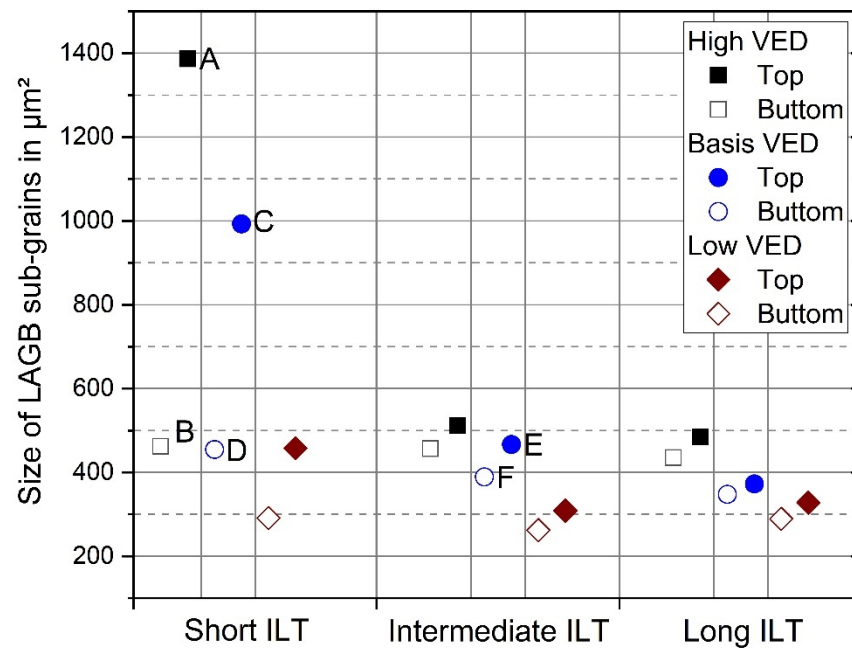


Figure 8. Comparison of sub-grain sizes (LAGB 5°) for each parameter combination. The capital letters correspond to the respective inverse pole figure maps in Figure 10.

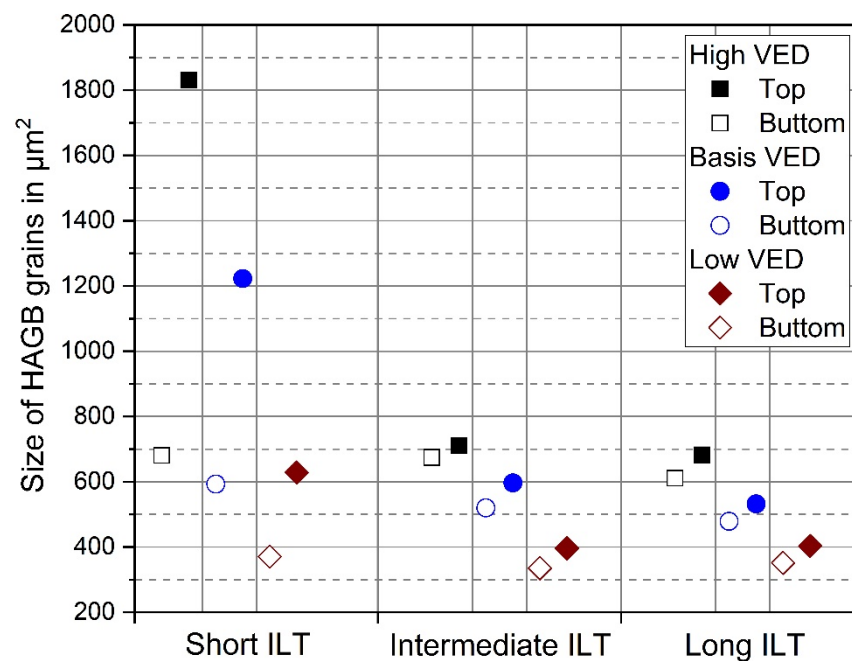


Figure 9. Comparison of grain sizes (HAGB 15°) for each parameter combination.

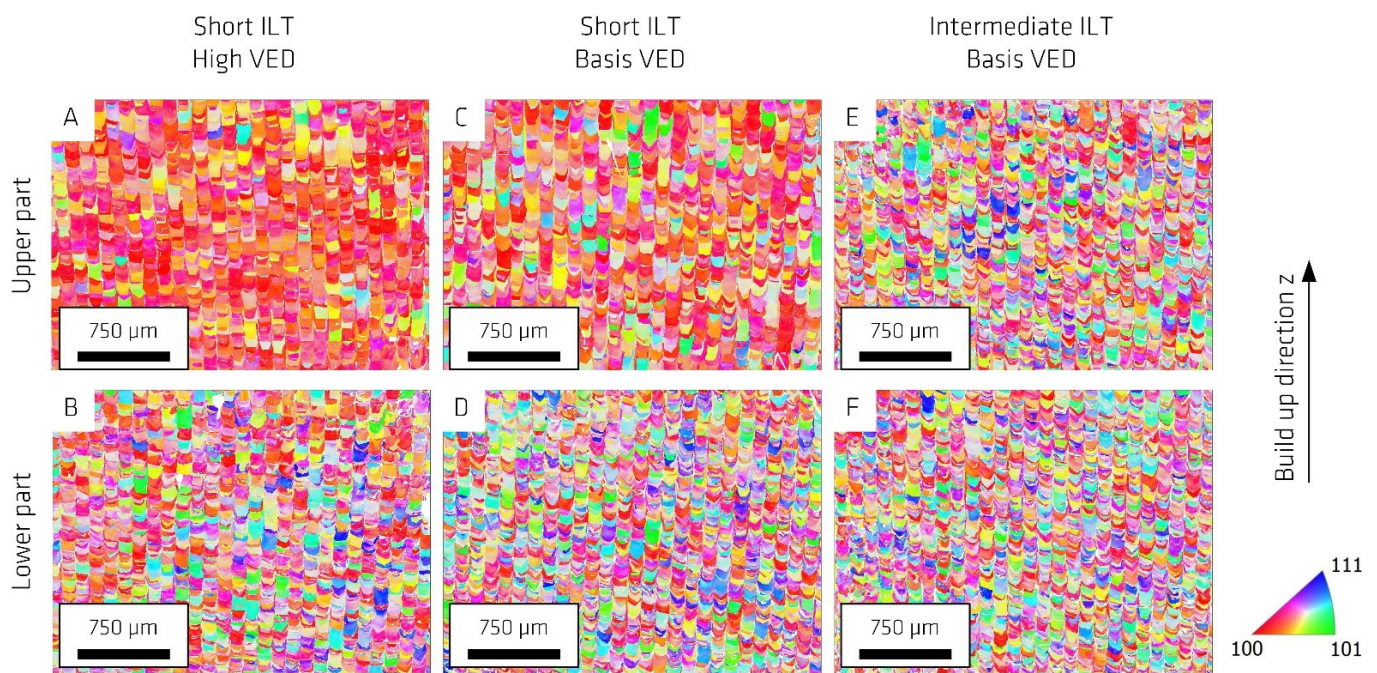


Figure 10. Inverse pole figure maps comparison with crystallographic orientation related to direction normal to the map plane. The capital letters correspond to the respective sub-grain sizes in Figure 8.

The measured grain size distribution is not Gaussian but follows a log-normal distribution. Hence, the mean and the standard deviation were calculated from logarithmic transformed measuring data. When retransformed, the standard deviation has to be considered multiplicatively, which results in asymmetric error bars with pronounced overlapping upper parts for the individual measuring points. Despite significant overlapping, the changes in the mean values are to be discussed. The mean values and standard deviations of the individual data points presented in Figures 8 and 9 are additionally given in Tables 5 and 6.

Table 5. LAGB sub-grain sizes.

| ILT | VED | sub-Grain Size in μm^2 Lower Part | | Sub-Grain Size in μm^2 Upper Part | |
|--------------|-------|---|--------------------|---|--------------------|
| | | Mean Value | Standard Deviation | Mean Value | Standard Deviation |
| Short | High | 462.4 | 3.6 | 1386.4 | 5.1 |
| | Basis | 454.6 | 4.0 | 992.9 | 5.3 |
| | Low | 291.5 | 3.2 | 457.7 | 4.5 |
| Intermediate | High | 456.8 | 4.2 | 511.4 | 4.4 |
| | Basis | 389.4 | 3.7 | 466.5 | 4.0 |
| | Low | 262.5 | 3.1 | 308.8 | 3.3 |
| Long | High | 435.2 | 4.0 | 484.5 | 4.2 |
| | Basis | 347.6 | 3.6 | 532.3 | 4.2 |
| | Low | 289.4 | 3.2 | 403.4 | 3.8 |

Table 6. HAGB grain sizes.

| ILT | VED | Grain Size in μm^2 Lower Part | | Grain Size in μm^2 Upper Part | |
|--------------|-------|---|--------------------|---|--------------------|
| | | Mean Value | Standard Deviation | Mean Value | Standard Deviation |
| Short | High | 689.9 | 4.1 | 1830.6 | 5.9 |
| | Basis | 592.6 | 4.3 | 1222.5 | 5.8 |
| | Low | 370.9 | 3.5 | 628.6 | 5.0 |
| Intermediate | High | 674.2 | 4.6 | 709.9 | 4.8 |
| | Basis | 520.0 | 4.0 | 596.2 | 4.3 |
| | Low | 335.2 | 3.4 | 396.4 | 3.7 |
| Long | High | 610.4 | 4.3 | 682.0 | 4.6 |
| | Basis | 478.6 | 4.0 | 532.3 | 4.2 |
| | Low | 351.2 | 3.4 | 403.4 | 3.8 |

3.3. Cellular Substructure

The SEM images revealed a cellular growth mode for all examined parameter combinations. The intersection counts as well as the calculated average cell size are depicted in Figure 11. Although there are huge overlapping areas of the deviation bars, two trends can be recognized from the results, as they appear consistently. First, the cellular size appears to be increased at the upper part of the specimens manufactured at short ILT for all VED levels. At the same time, no differences can be noticed between upper and lower part at longer ILT and standard VED. Second, the cell size increases with increasing VED (decreasing scanning velocity v_s) irrespective of the build height. This can only be reported for the short ILT level, as for the other ILT levels only the standard VED was considered in this measurement. The average cell size within this investigation is between 0.52 μm and 0.76 μm .

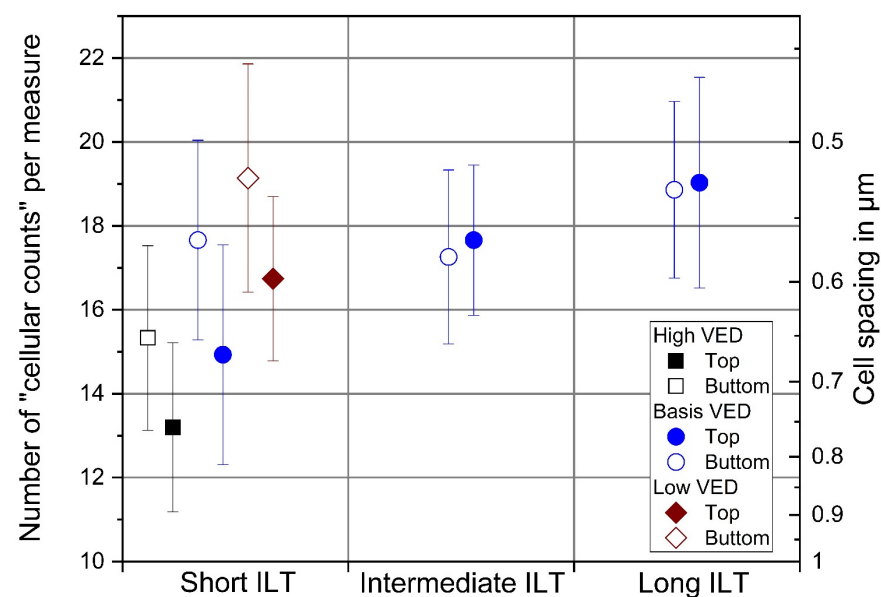


Figure 11. Comparison of cell spacing intersection counts for different parameter combinations. The right y-axis corresponds to the calculation of the cell spacing.

3.4. Chemical Composition

The EBSD measurements showed no hint for phases other than austenite. The measured chemical composition of the examined specimens is depicted in Table 7.

Table 7. Chemical composition of selected specimens in weight %.

| Element | Uncertainty | Short ILT High VED | | Short ILT Basis VED | | Intermediate ILT Basis VED | | Long ILT Low VED | |
|---------|-------------|-----------------------|------------|------------------------|------------|-------------------------------|------------|---------------------|------------|
| | | Lower Part | Upper Part | Lower Part | Upper Part | Lower Part | Upper Part | Lower Part | Upper Part |
| C | 0.0020 | 0.0149 | 0.0142 | 0.0161 | 0.0152 | 0.0156 | 0.0159 | 0.0168 | 0.0171 |
| Si | 0.05 | 0.59 | 0.59 | 0.61 | 0.52 | 0.55 | 0.52 | 0.62 | 0.56 |
| Mn | 0.03 | 0.89 | 0.92 | 0.91 | 0.94 | 0.87 | 0.90 | 0.91 | 0.94 |
| Cr | 0.4 | 17.9 | 17.9 | 18.0 | 17.9 | 17.9 | 18.0 | 17.9 | 17.9 |
| Mo | 0.04 | 2.38 | 2.40 | 2.42 | 2.39 | 2.37 | 2.42 | 2.39 | 2.41 |
| Ni | 0.3 | 12.8 | 12.8 | 12.9 | 12.8 | 12.7 | 12.9 | 12.8 | 12.9 |
| N | 0.005 | 0.075 | 0.077 | 0.078 | 0.077 | 0.079 | 0.078 | 0.082 | 0.083 |
| P | 0.002 | 0.008 | 0.009 | 0.010 | 0.009 | 0.008 | 0.009 | 0.009 | 0.009 |
| S | 0.0004 | 0.0043 | 0.0041 | 0.0042 | 0.0043 | 0.0042 | 0.0042 | 0.0042 | 0.0042 |
| Fe | - | bal. | bal. | bal. | bal. | bal. | bal. | bal. | bal. |

The measured chemical composition of the examined specimens was compared to the material specification listed in Table 1. In all cases, the chemical composition meets the specifications. The chemical composition of the lower part was compared to the chemical composition of the upper part for each specimen and for each chemical element. Considering the measurement uncertainty, no significant differences between the upper and lower part of each specimen can be recognized. In addition, no significant differences to the chemical composition of the powder can be recognized.

The results of the measurement of the oxygen content conducted at two separate specimens are depicted in Table 8.

Table 8. Oxygen content in weight %.

| Measurement Uncertainty | Short ILT High VED | | Intermediate ILT Basis VED | |
|----------------------------|-----------------------|------------|-------------------------------|------------|
| | Lower Part | Upper Part | Lower Part | Upper Part |
| 0.004 | 0.036 | 0.034 | 0.031 | 0.031 |

4. Discussion

4.1. Surface Temperatures

The preheating temperature plots reveal three clear trends. First, the preheating temperature increases over the entire build height of the specimens. This confirms similar results from previous work [5] and the work of Williams et al. [34]. As long as the preheating temperature rises over the build height, there is no equilibrium between the rate of heat input and the rate of heat dissipation [34]. Heat dissipates mainly by thermal conduction into the build and the base plate due to strong insulating effects of the surrounding powder [22]. Therefore, the heat dissipation is mainly governed by thermal conductivity and the geometry of the build. For a constant geometry and a given material, the heat dissipation via heat conduction can be shortened by reducing the time before the next energy input, i.e., by reducing the ILT.

This directly leads to the second trend observed in the plots: the increase of preheating temperature is significantly affected by a change of the time for heat dissipation through varying ILT. Shorter ILTs allow for a shorter time for heat dissipation resulting in increasing

preheating temperatures. A massive heat accumulation is observable in the most extreme case (short ILT and high VED) of the parameter matrix, leading to temperatures of up to approximately 600 °C. In contrast, the preheating temperature in the least extreme case (long ILT and low VED) level was up to approximately 140 °C. The magnitude of this intrinsic preheating effect is material-specific due to material-specific thermal conductivity. It would be expected to be reduced for materials with higher thermal conductivity.

Third, the increase of preheating temperature also depends significantly on the energy input varied by the distinct processing parameters. This results in increased temperatures at a reduced scanning velocity. It is well known that the energy input is higher at slower scanning velocities resulting in higher specimen temperatures [40,41].

Oxidation layers may drastically change the emissivity of metallic surfaces, which is a well-known phenomenon [42]. Oxidation phenomena were argued to be responsible for drastic changes in emissivity values at temperatures above 580 °C in the previously conducted experiments for the determination of emissivities [35]. Furthermore, oxidation-driven tempering colors could be noticed for short ILT specimens, especially for those at basis VED and high VED [5]. Therefore, the interpretation of calculated temperatures above 580 °C should be considered very carefully in this study. However, there are two aspects that back the reliability of the measured temperature values despite oxidation of the specimen's bulk surface. First, oxidation thickness growth depends always on atmosphere, temperature and time [35]. The atmosphere can be assumed to be the same for all individual specimens of the different ILT levels, as they were produced within the same build process with a low oxygen content (below 0.1% [5]). The suspect temperatures are not far beyond the revealed detrimental temperature threshold of 580 °C. The time for oxidation of the recoated powder layer before the measurement signal extraction is comparably short, i.e., below 15 s in the case of the L-PBF process with short ILT. In comparison, Janssen [43] studied oxidation processes at austenitic stainless steel AISI 304 in air and noticed the start of slight yellow annealing colors by eye at 550 °C at 5 min holding time. In addition, the new recoated powder layer did not undergo the temperature cycle of the L-PBF bulk material. Therefore, it did not face very high temperatures prone to oxidation. Second, the relative comparison of the preheating temperatures of the distinct VED levels shows a constant ratio irrespective of the individual ILT. Hence, within the light of the given measurement uncertainty, the presented temperature values can be directly used for comparison. Potential oxidation is assumed to not have affected the emissivity of the powder surface significantly before the recording of the extracted IR signal.

4.2. Grain Size Analysis

Three clear trends can be derived from the measurements: First, HAGB grain sizes and LAGB sub-grain sizes show the same qualitative differences regarding VED, ILT and build height. Second, the grain sizes and, respectively, the sub-grain sizes increased with increasing VED for every ILT. Third, for every parameter combination, the upper part sections exhibit a higher grain size and sub-grain size as compared to the lower sections. However, this increase is small for long ILT and intermediate ILT compared to short ILT specimens. For the short ILT specimens, the difference in mean grain sizes, respectively, mean sub-grain sizes, can be higher than a factor of two, as can be seen for basis VED and high VED. The measured mean HAGB grain sizes as well as mean LAGB grain sizes are in the same order of magnitude as examined elsewhere.

In the previous publication [5], no significant difference in mean values of the sub-grain sizes of the lower part sections and upper part sections of the short ILT specimens could be examined by the applied manual measurement via line interception of light microscopy images. This was obviously due to a very high degree of measurement uncertainty. An in-situ heat treatment during the process was proposed as a potential explanation. However, this proposition can now be clearly disproven by the EBSD results, as clear differences in the mean grain size and the mean sub-grain size between upper and lower part can be seen whenever the preheating temperature was also increased strongly. The average

preheating temperature of each specimen between layer 2140 and layer 2200, which is within the upper part sections, and the LAGB sub-grain sizes are depicted within the same diagram in Figure 12. This visualizes the high degree of correlation between the preheating temperature as a boundary condition for solidification and grain size development. The noticeable discrepancy between a comparatively high preheating temperature and still small mean grain size in the specimen of short ILT and low VED as compared to, e.g., the specimen of long ILT and high VED, should not be considered without referring to changes in melt pool depth as presented in [5]. The preheating temperature shows an effect on the development of the microstructure. The latter is also known to be strongly affected by the melt pool dimensions [3], which are comparatively small for the low VED value due to the higher scanning velocity [5]. Therefore, the temperature influence should be rather considered within the individual VED levels for direct comparison.

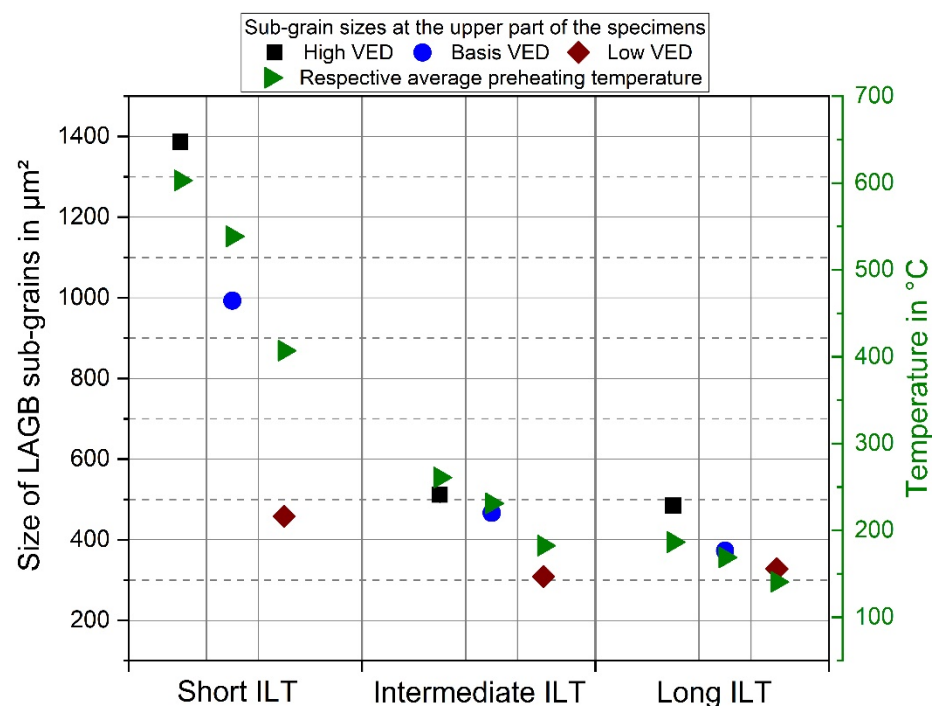


Figure 12. Comparison of LAGB sub-grain sizes and preheating temperatures for each parameter combination in the upper part sections. The preheating temperature values depict the average of the measured preheating temperature of the respective specimen between layer 2140 and 2200.

4.3. Cellular Substructure

The calculated average cell size is in the same order of magnitude as reported in other literature, where cell sizes in the range of 0.5 μm to 1 μm or 1.5 μm, depending on processing parameters, were measured [15,39,44,45]. Leicht et al. [46] presented slightly smaller cell sizes in a range of 0.36 μm to 0.58 μm.

Roehling et al. [30] described the propagation rate of the solid liquid interface being linked with the scanning velocity by its product with the cosine of the angle between the laser scanning direction and the solidification direction. Typical values are in the range of 0.012 m·s⁻¹ to 0.12 m·s⁻¹ and, therefore, significantly smaller than the scanning velocity v_s [9]. These values can be estimated for scanning velocities of about 700 mm·s⁻¹ assuming an angle between the direction of the maximum heat flow and the build direction between 0° and 10°, as supposed by DebRoy et al. [3]. Thermal gradients G are reported in the range from 10⁴ K·m⁻¹ to 10⁷ K·m⁻¹ and being rather at the top of this range in the case of L-PBF as compared to direct energy deposition [9]. Pinomaa et al. [9] conducted a phase field simulation of the rapid directional solidification of 316L and measured the cell sizes for different local melt pool solidification rates R and different thermal gradients G . They

examined a clear cellular growth mode of solidification over a broad range of the typically reported thermal gradient ranges and solidification rates [9].

In the case of cellular growth mode, which also appeared in the examined specimens of the present study, a general trend of a decrease of the cellular size with increasing solidification rate as well as increasing thermal gradients could be revealed from the work of Pinomaa et al. [9]. Their 2D phase field model brought up cell sizes in the range of 0.64 μm to 4.1 μm for the pure cellular growth mode. When comparing the values of Figure 11 to their simulation results, the figures are again in the same order of magnitude for their higher R and different thermal gradients G . Qualitatively, the relationship between increasing cell size with decreasing thermal gradients tends to appear for the short ILT, suggesting that the increased preheating temperature (see Figure 4) decreased the thermal gradient of cooling. Additionally, at lower scanning velocities v_s (higher VED) the cell size increased accordingly.

The good agreement to the simulation results, published in [9], seems to be surprising since the melt pool geometry is reported to have a huge impact on the heat and mass transfer within the melt pool [47,48]. Differences in melt pool depth were examined for the varying processing conditions in the previous study [5]. In addition, the solidification rate R as well as the local thermal gradient G vary over the cross section of the melt pool [30,47,48]. Yadroitsev et al. [49] have shown the sensitivity of the cell spacing to the scanning velocity and the location of measurement within single track melt pools. At a first glance, this would appear to complicate valid comparisons of cell size measurements as the selection of the measurement region within the cross sections might affect the result strongly. In fact, the measurement regions in the SEM images of the same cross section subjectively appeared to show huge variation in the cell size. This is assumed to be the reason for the comparably huge deviation bars in Figure 11, as similarly concluded by Leicht et al. [46]. However, the potential melt pool cross section areas to be investigated within the bulk of the specimens are limited to fragments of the lower part of the melt pool in this study. This is due the layer-wise remelting and overlapping of melt pools. Yadroitsev et al. [49] measured gradual increasing differences in cell spacing of up to a factor of 2 between upper and lower part of the melt pool. A comparison of the lower part and the middle section of the melt pool showed only a difference of a factor of 1.3. Therefore, it can be assumed that the variations in the measurable cell spacings are reduced due to remelting. Additionally, it is assumed that the primary solidification structures remain stable and are not affected significantly in any secondary heat cycle. This was also one of the critical model assumptions of the phase field simulation by Pinomaa et al. [9].

Deng et al. [39] conducted recently very fundamental investigations on the thermal stability of the cellular substructure which consists of dislocations. They hold 316L L-PBF specimens at elevated temperatures of 500 $^{\circ}\text{C}$, 600 $^{\circ}\text{C}$, and 700 $^{\circ}\text{C}$ for up to 150 h. No recrystallization was observed at these temperatures. They eliminated a lack of knowledge about the behavior of the dislocation network at elevated temperatures below the often-reported dislocation dissolution temperatures above 850 $^{\circ}\text{C}$ [16]. The cellular substructure remains stable at 600 $^{\circ}\text{C}$ for up to 100 h. At 700 $^{\circ}\text{C}$, the decomposition of the dislocation cells was already visible after a 10 h annealing. The dislocation cells showed a uniform growth along all directions at this heating condition. This growth was related to a rearrangement and coarsening of dislocation structures. It did not occur homogeneously over the entire cross section areas that were investigated. The growth proceeded very slightly when increasing the annealing time up to 150 h. The findings of Deng et al. [39] exclude a potential in-situ annealing effect as a reason for the measured differences in the cell spacing in this study. This was suggested as a potential reason for differences in hardness values in the previous study [5]. However, this does not apply since the measured preheating temperatures are well below the threshold of 700 $^{\circ}\text{C}$. Therefore, the differences in the feature size of the cellular substructure of this study are assumed to completely develop during solidification. This also supports the consideration of differences of G and R for being the main cause of the differences in feature size as discussed above.

4.4. Chemical Composition

No significant differences between the upper and lower part of each specimen or to the chemical composition of the powder can be recognized. However, small differences in the oxygen content of the “short ILT, high VED” specimen and the “intermediate ILT, basis VED” specimen are detected. Although these differences (0.003 weight % to 0.005 weight %) barely exceed the measurement uncertainty, a closer look into these differences seems to be reasonable.

At the first glance, this would even correlate well with the different preheating temperatures (see Figures 4 and 5) of the parts examined here and with the different annealing colors at the outer surfaces of the specimens observed in [5]. However, looking in more detail, such a perceived view cannot explain the difference between the lower part of the short ILT specimen and the upper part of the intermediate ILT specimen. Both face similar preheating conditions as shown in Section 3.1. It cannot explain a perceived slightly higher oxygen content in the lower part of the short ILT specimen compared to its upper part, although oxidation of the L-PBF surface in its upper part was clearly visible. In addition, the preheating temperatures were in a temperature range prone to surface oxidation. Surface oxides were not measured in the oxygen analysis since hydrochloric acid etching was conducted before the measurement. Hence, only the oxygen intake in the bulk material was measured.

However, short ILT and intermediate ILT specimens were manufactured in two different processes. Therefore, the logging data of the internal oxygen lambda probes of the L-PBF system have to be examined. As the experienced L-PBF user of this specific machine knows, the process starts when the residual oxygen concentration in the process chamber is below 0.1%. For the working principle of the gas flushing regarding the maintenance of a low oxygen content, one is referred to the detailed explanation given by Pauzon et al. [50] for another L-PBF machine with a similar principle. After reaching 0.1%, the concentration measured at the lambda probes usually levels down in the beginning of the process to approximately 0.02%. Figures 13 and 14 depict the oxygen concentration in the atmosphere of the process chamber during the first 300 min of the short ILT process and intermediate ILT process respectively. The upper x-axis of these plots shows the respective build height, which must be substantially higher within the same process time for short ILT. It can be derived from the two diagrams that the residual oxygen content during manufacturing of the lower ex-situ volumes of analysis (build height between 2.5 mm and 12.5 mm, see Figure 1) was higher for the short ILT process compared to the intermediate ILT process. Therefore, this can be presumed to cause the higher weight % of oxygen in the lower part of the short ILT specimen measured by chemical analysis, as listed in Table 8. This can be supported by findings of similar magnitude by Dietrich et al. [51]. They reported an increase in oxygen content by 0.0188 weight % in L-PBF Ti6Al4V bulk material manufactured in a process chamber atmosphere of 0.0977 weight % oxygen concentration compared to a process with 0.0002 weight % oxygen concentration.

The reason for the difference in the time span until the oxygen content in the process chamber leveled down cannot be clarified within the frame of the experimental set-up of this study. Potentially, the residual oxygen consumption in the process chamber is affected by the number of parts or (more precisely) the ratio of area exploitation. While only the three specimens, which were in the field of view of the IR camera, were manufactured in the short ILT process, additional 15 specimens of the same size were manufactured in the intermediate ILT process. Hence, the faster decrease of residual oxygen concentration during the build-up could be related to a bigger surface area available for oxygen intake in the intermediate ILT process.

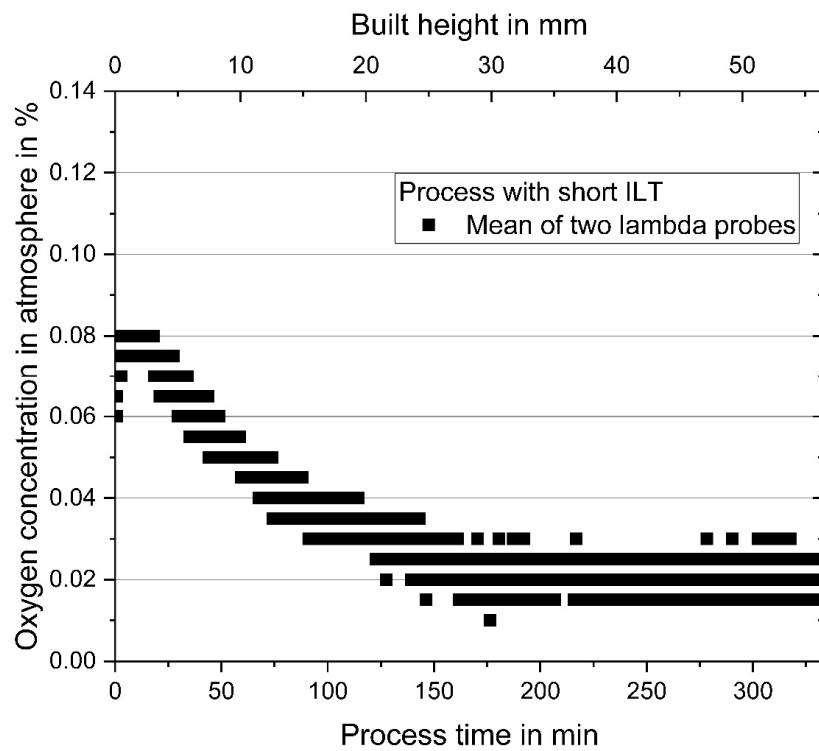


Figure 13. Oxygen concentration in the process chamber during the first 300 min of the short ILT process.

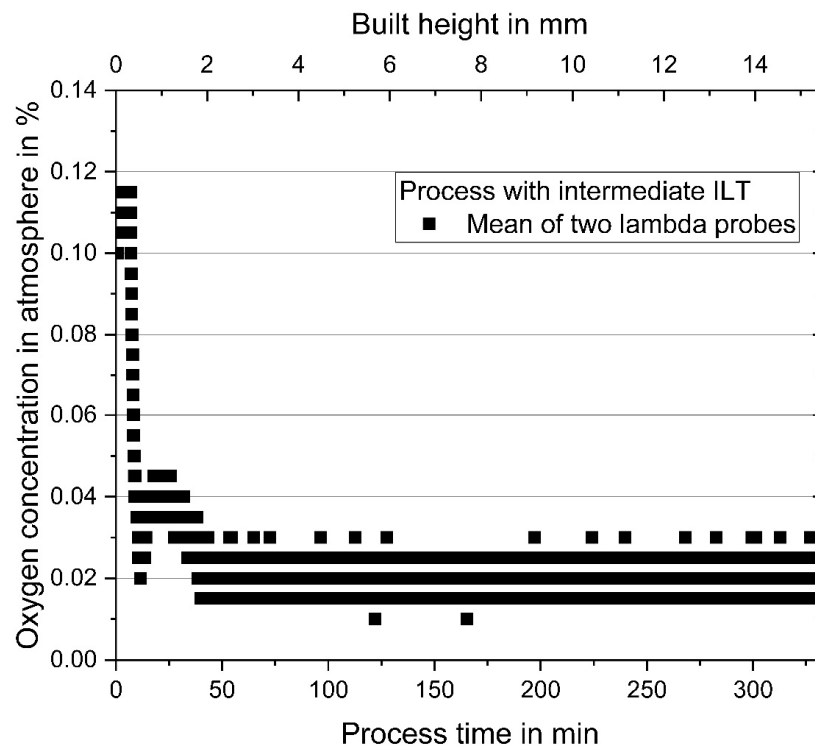


Figure 14. Oxygen concentration in the process chamber during the first 300 min of the intermediate ILT process.

After leveling down of the oxygen concentration in the process chamber to approximately 0.02%, these values kept constant over the rest of each build process. Hence, the small differences in the upper part of the two specimens, which are smaller than the measurement uncertainty, could be a result of higher oxygen intake into the L-PBF

bulk due to different preheating temperatures. The specimens with shorter ILT showed slightly higher oxygen content than specimens with longer ILT. This suggestion can be supported by recent findings of Pauzon et al. [52]. They reported that a reduced ILT can lead to increased oxygen pick-up during L-PBF manufacturing of Ti6Al4V specimens. They measured differences in oxygen pick-up of approximately 0.05 weight % for specimens at 70 mm build height manufactured with different ILT, when the oxygen concentration in the process atmosphere was below 0.1 weight %. However, as the measurement uncertainty is high in comparison to the discussed difference, further examinations should be done in future work.

The measured quantities of oxygen content are well within the range of published values in the literature for the same material and process. A recent study from Pauzon et al. [50], dedicated to process gas influence during L-PBF processing of 316L, revealed oxygen concentrations of approximately 0.0424 weight % in the bulk of their specimens. This is not only in good agreement in terms of magnitude but also quite close to the values examined here. Lou et al. [23] measured an oxygen content of about 0.0384 weight % at 316L L-PBF specimens. Pauzon [53] also highlighted the solubility limit of oxygen in austenite being estimated by Kitchener et al. [54] at about 0.003 weight % \pm 0.003 weight %. Oxygen content above this value is expected to be connected to secondary phase oxide inclusions, mainly with elements such as Cr, Mn, or Si [53]. Hints about the existence of such nanosized precipitations in 316L can be found, e.g., in the work of Liverani et al. [17], Saedi et al. [55], and Sun et al. [18]. Krakhmalev et al. [16] described the size of these particles in the range of 15 nm to 100 nm. Detrimental influences on impact toughness were discussed by Lou et al. [23].

4.5. Subsumption of the Results with Regard to Hardness

In this section, the variations of the analyzed features are discussed with regard to hardness values obtained in the previous study [5]. A significant hardness drop in the upper part sections of the short ILT specimens as compared to the lower part sections was revealed [5], despite relatively low defect densities. At intermediate ILT, only a slight decrease in hardness over the build height was recognized. The range of hardness values was at a similar level in the upper and the lower part sections at long ILT. The hardness values in the upper part sections are transcribed from [5] into a diagram that again shows the sub-grain sizes of the respective upper parts, see Figure 15. The hardness values are discussed in the following as representative for material strength. The strength of metallic materials is the sum of the following contributions: contributions from dislocations, from grain boundaries, from solid solutions, and from precipitations [56]. Hence, the identified differences in grain sizes as well as in cell spacing should be discussed with respect to hardness.

An inverse relationship between hardness values and LAGB sub-grain sizes can be seen in the direct comparison diagram in Figure 15. The same relationship would be visible also for the HAGB grain sizes, as a comparison between the results in Section 3.2 indicates (see Figures 8 and 9). Both microstructural feature sizes seem to obey a Hall-Petch type relationship between grain sizes and material strength. However, as reported at many places the high dislocation density of the cellular substructure within the sub-grains plays an additional and very important role in strengthening of 316L material produced by L-PBF [9,15,39,57]. Besides the measured grain sizes, the measured cell spacing also shows an inverse relationship regarding hardness. For the most extreme parameter combination (short ILT, high VED, and upper part), a contribution of keyhole porosity to the hardness drop cannot be excluded entirely [5]. However, for all other specimens the defect density was low enough for not being assumed to affect hardness.

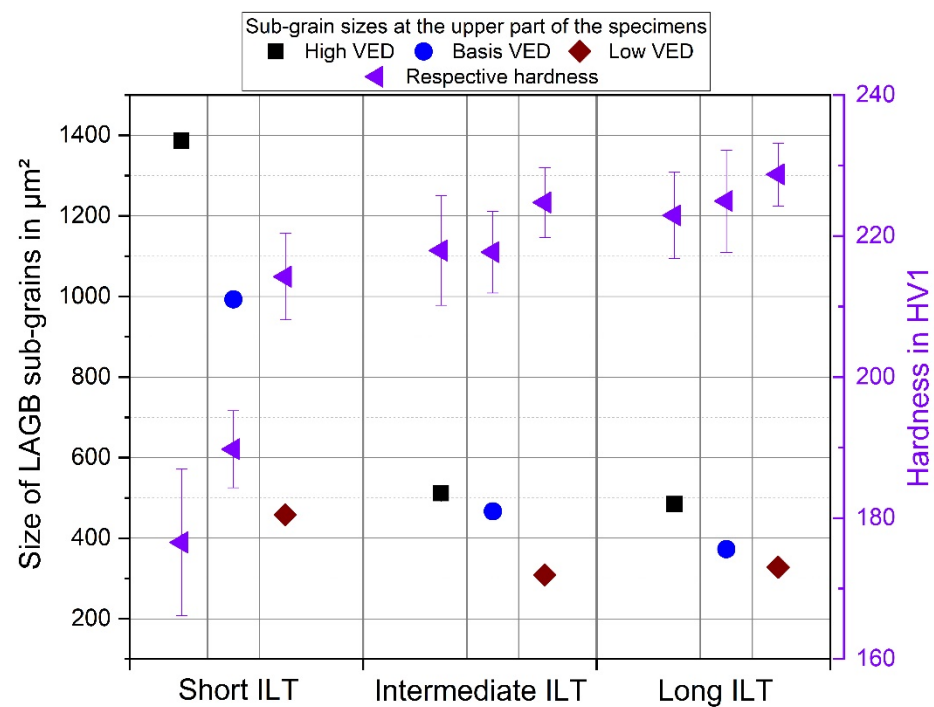


Figure 15. Comparison of LAGB sub-grain sizes of the upper part sections and the respective hardness values (Adapted from ref. [5]) for each parameter combination.

Deng et al. [39] conducted very fundamental annealing experiments. They showed that a decrease in hardness already appears before the onset of any recrystallization as a matter of changes in dislocation cell size. Under the assumption of changes in dislocation cell size only, the cell size is allowed to be used for a direct correlation to strength based on a Hall-Petch relationship as proofed valid by Deng et al. [39]. However, they also showed that the correlation factor k , which is normally assumed to be a constant factor in a Hall-Petch type relationship, can change non-linearly due to different dislocation annihilation behavior depending, e.g., on the annealing time. This is already relevant below the starting temperature of a complete annihilation of dislocations, below 800 °C. In simplified terms, not only the cell size of the dislocation structure but also the dislocation density within the cell boundaries contribute to the material strength. However, this can only be studied by intense use of transmission electron microscopy.

A direct transfer from the annealing experiments of Deng et al. [39] to the results of the present study does not work since it can be assumed that the differences in microstructural features of the specimens of this study are not caused by annealing but by differences in the initial conditions of solidification. This assumption is supported by differences in grain sizes between upper part and lower part sections of the same specimens as discussed in Section 4.2. This cannot be the result of any recrystallization or annealing grain growth, as otherwise the cellular substructure would have been dissolved. Therefore, the primary cause of the differences in the feature size of the cellular structure as well as in the LAGB and HAGB grain sizes is assumed to be related to the differences in solidification rate and thermal gradients. Both are affected by the interplay of VED and ILT variations as well as by the build height. The evolution of the preheating conditions over the build height for the different parameter combinations clearly indicates a change of the initial thermal conditions of solidification. An increase of grain size with decreasing cooling rates was already reported by Zitelli et al. [1] and Keshavarzkermani et al. [14].

Interestingly, Bang et al. [58] recently investigated changes in microstructure and hardness i.a. of small 10 mm cubic L-PBF specimens of 316L over a broad range of parameter combinations of laser power (80 W to 480 W) and scanning velocity (493 mm·s⁻¹ to 2958 mm·s⁻¹). For all parameter combinations with resulting high density, their mi-

microstructural characterization revealed an increase of cell size and grain size in proportion to the applied VED except for one outlier at the highest VED condition. A decrease in hardness from approximately 220 HV0.5 to approximately 180 HV0.5 was exhibited with increasing VED, which they related to the inverse relationship between hardness and grain sizes. As mentioned elsewhere, a direct comparison of VED values is not acceptable in its entirety and has to be done very carefully, see, e.g., [59,60]. However, when considering a comparison of the hardness values of Bang et al. [58] with the values of the present study—its pre-study [5]—it becomes clear that Bang et al. [58] used a much broader range of processing parameters (laser power and scanning velocity) than in the present study. Thereby, they provoked similar conditions in terms of resulting hardness and trends of increasing microstructural feature size at their 10 mm cubic specimens. These conditions were induced by a relatively narrow variation of the VED in combination with an application relevant build height of over 100 mm and decreasing ILTs in the present study.

This in total emphasizes the importance of ILT in combination with build height on the development of the microstructure and the resulting mechanical properties in L-PBF, as together they seem to be able to drastically shift the processing window, gained from typical process parameter studies.

5. Conclusions

An in-depth analysis of the microstructural feature sizes of 316L specimens produced at different VED levels and different ILT levels has been conducted. Furthermore, the evolution of the intrinsic preheating temperature over the complete build-up of specimens was monitored by use of a thermographic in-situ monitoring set-up.

Several influencing factors and their implications have been identified.

1. Preheating temperature: An increase of VED can rise the preheating temperature as the heat input into the material is increased. The rise of preheating temperature by a decrease of ILT is much more significant. This is related to the reduced time for heat dissipation. Temperature measurements have revealed a change in preheating temperature by more than a factor of 2 in the upper part of the specimens for short ILT (18 s) compared to longer ILT (65 s and 116 s). Intrinsic preheating temperatures of up to about 600 °C were revealed. In turn, this resulted in heterogeneity of the microstructure and differences in material properties within the same specimen, as specified below.
2. Grain sizes: A significant increase of grain sizes and sub-grain sizes was identified in sections of specimens with increased preheating temperature. Differences in grain size of more than a factor of 2.5 were found within the same specimen, which was attributed to the variations in build height and parameter combination.
3. Spacing of cellular substructure: The measurement of cell spacing is handicapped by significant measurement uncertainty due to the high degree of local changes within very small areas, i.e., within the size of individual melt pools. Despite this scatter, a trend to increasing cell sizes was observed and was related to differences in solidification rate and thermal gradients induced by differences in scanning velocity and preheating temperature. The average cell size within this investigation was between 0.52 µm and 0.76 µm, depending on the parameter combination.
4. Hardness: Eventually, the examined and discussed differences in grain sizes and cell sizes were related to differences in hardness examined in a previous study [5]. A general trend of decreasing hardness (from 221 HV1 to 176 HV1) with increasing microstructural feature size was revealed.

Furthermore, there was a slight tendency of increasing oxygen intake in regions of high preheating temperature. However, the basis for these oxygen measurements is quite limited, and further investigations in this field are required. This will also include better control of the boundary conditions of oxygen content within the L-PBF process.

The findings of this study are strongly linked to intrinsic changes in preheating temperature during the L-PBF process. The causes of these significant changes were

identified to be related to processing parameters such as scanning velocity (affecting VED) but also to build height and ILT, which are overlooked in many other cases in the literature. When considering real part geometries and current trends in the development of new L-PBF machines (e.g., multi laser machines), a decrease in ILT can be expected during manufacturing. This will make the issue of differences in microstructure and mechanical properties due to intrinsic preheating temperature changes more severe. Therefore, the authors want to close with the recommendation to always include the ILT into the process documentation to enhance the comparability of measurement results of L-PBF products.

Author Contributions: Conceptualization, G.M.; methodology, G.M., K.S. and T.K.; software, G.M. and T.K.; validation, G.M., K.S. and T.K.; formal analysis, G.M., K.S., T.K. and S.R.; investigation, G.M., K.S., T.K. and S.R.; resources, S.J.A., K.H.; data curation, G.M., K.S. and T.K.; writing—original draft preparation, G.M., T.K.; writing—review and editing, G.M., K.S., T.K., S.J.A., S.R., D.B. and K.H.; visualization, G.M.; supervision, K.H.; project administration, S.J.A. All authors have read and agreed to the published version of the manuscript.

Funding: This research was funded by BAM within the focus area materials.

Institutional Review Board Statement: Not applicable.

Informed Consent Statement: Not applicable.

Data Availability Statement: Not applicable.

Acknowledgments: The authors would like to thank M. Ostermann for XRF measurements, A. Meckelburg for determination of non-metals, J. Roik for ICP-OES measurements, R. Saliwan Neumann for SEM images, and A. Charmi for support in generating IPF maps.

Conflicts of Interest: The authors declare no conflict of interest. The funders had no role in the design of the study; in the collection, analyzes, or interpretation of data; in the writing of the manuscript; or in the decision to publish the results.

References

1. Zitelli, C.; Folgarait, P.; di Schino, A. Laser powder bed fusion of stainless steel grades: A review. *Metals* **2019**, *9*, 731. [[CrossRef](#)]
2. Gralow, M.; Weigand, F.; Herzog, D.; Wischeropp, T.; Emmelmann, C. Biomimetic design and laser additive manufacturing—A perfect symbiosis? *J. Laser Appl.* **2020**, *32*, 021201. [[CrossRef](#)]
3. DebRoy, T.; Wei, H.L.; Zuback, J.S.; Mukherjee, T.; Elmer, J.W.; Milewski, J.O.; Beese, A.M.; Wilson-Heid, A.; De, A.; Zhang, W. Additive manufacturing of metallic components—Process, structure and properties. *Prog. Mater. Sci.* **2018**, *92*, 112–224. [[CrossRef](#)]
4. Wycisk, E.; Munsch, M.; Schmidt-Lehr, M. *AMPOWER Report 2021: Additive Manufacturing Market*; Report; AMPOWER GmbH & Co. KG: Hamburg, Germany, 2021.
5. Mohr, G.; Altenburg, S.J.; Hilgenberg, K. Effects of inter layer time and build height on resulting properties of 316L stainless steel processed by laser powder bed fusion. *Addit. Manuf.* **2020**, *32*, 101080. [[CrossRef](#)]
6. Sanaei, N.; Fatemi, A.; Phan, N. Defect characteristics and analysis of their variability in metal L-PBF additive manufacturing. *Mater. Des.* **2019**, *182*, 108091. [[CrossRef](#)]
7. Gorelik, M. Additive manufacturing in the context of structural integrity. *Int. J. Fatigue* **2017**, *94*, 168–177. [[CrossRef](#)]
8. Zerbst, U.; Bruno, G.; Buffiere, J.-Y.; Wegener, T.; Niendorf, T.; Wu, T.; Zhang, X.; Kashaev, N.; Meneghetti, G.; Hrabe, N.; et al. Damage tolerant design of additively manufactured metallic components subjected to cyclic loading: State of the art and challenges. *Prog. Mater. Sci.* **2021**, 100786. [[CrossRef](#)]
9. Pinomaa, T.; Lindroos, M.; Walbrühl, M.; Provas, N.; Laukkanen, A. The significance of spatial length scales and solute segregation in strengthening rapid solidification microstructures of 316L stainless steel. *Acta Mater.* **2020**, *184*, 1–16. [[CrossRef](#)]
10. Mohr, G.; Scheuschner, N.; Hilgenberg, K. In situ heat accumulation by geometrical features obstructing heat flux and by reduced inter layer times in laser powder bed fusion of AISI 316L stainless steel. *CIRP Proceedings* **2020**, *94*, 155–160. [[CrossRef](#)]
11. Seifi, M.; Gorelik, M.; Waller, J.; Hrabe, N.; Shamsaei, N.; Daniewicz, S.; Lewandowski, J.J. Progress towards metal additive manufacturing standardization to support qualification and certification. *Jom* **2017**, *69*, 439–455. [[CrossRef](#)]
12. Ranjan, R.; Ayas, C.; Langelaar, M.; van Keulen, F. Towards design for precision additive manufacturing: A simplified approach for detecting heat accumulation. In Proceedings of the Advancing Precision in Additive Manufacturing: 2018 ASPE and EUSPEN Summer Topical Meeting, Berkely, CA, USA, 22–25 July 2018.
13. Ranjan, R.; Ayas, C.; Langelaar, M.; van Keulen, F. Fast detection of heat accumulation in powder bed fusion using computationally efficient thermal models. *Materials* **2020**, *13*, 4576. [[CrossRef](#)]

14. Keshavarzkermani, A.; Marzbanrad, E.; Esmaeilizadeh, R.; Mahmoodkhani, Y.; Ali, U.; Enrique, P.D.; Zhou, N.Y.; Bonakdar, A.; Toyserkani, E. An investigation into the effect of process parameters on melt pool geometry, cell spacing, and grain refinement during laser powder bed fusion. *Opt. Laser Technol.* **2019**, *116*, 83–91. [[CrossRef](#)]
15. Wang, Y.M.; Voisin, T.; McKeown, J.T.; Ye, J.; Calta, N.P.; Li, Z.; Zeng, Z.; Zhang, Y.; Chen, W.; Roehling, T.T.; et al. Additively manufactured hierarchical stainless steels with high strength and ductility. *Nat. Mater.* **2018**, *17*, 63–71. [[CrossRef](#)] [[PubMed](#)]
16. Krakhmalev, P.; Fredriksson, G.; Svensson, K.; Yadroitsev, I.; Yadroitsava, I.; Thuvander, M.; Peng, R. Microstructure, solidification texture, and thermal stability of 316 L stainless steel manufactured by laser powder bed fusion. *Metals* **2018**, *8*, 643. [[CrossRef](#)]
17. Liverani, E.; Toschi, S.; Ceschini, L.; Fortunato, A. Effect of selective laser melting (SLM) process parameters on microstructure and mechanical properties of 316L austenitic stainless steel. *J. Mater. Process. Technol.* **2017**, *249*, 255–263. [[CrossRef](#)]
18. Sun, Z.; Tan, X.; Tor, S.B.; Yeong, W.Y. Selective laser melting of stainless steel 316L with low porosity and high build rates. *Mater. Des.* **2016**, *104*, 197–204. [[CrossRef](#)]
19. Aggarwal, A.; Patel, S.; Kumar, A. Selective laser melting of 316L stainless steel: Physics of melting mode transition and its influence on microstructural and mechanical behavior. *Jom* **2018**, *71*, 1105–1116. [[CrossRef](#)]
20. Patel, S.; Vlasea, M. Melting modes in laser powder bed fusion. *Materialia* **2020**, *9*, 100591. [[CrossRef](#)]
21. David, S.; Vitek, J.; Reed, R.; Hebble, T. *Effect of Rapid Solidification on Stainless Steel Weld Metal Microstructures and Its Implications on the Schaeffler Diagram*; Technical Report; Oak Ridge National Lab.: Oak Ridge, TN, USA, 1987.
22. Bajaj, P.; Hariharan, A.; Kini, A.; Kürnsteiner, P.; Raabe, D.; Jäggle, E.A. Steels in additive manufacturing: A review of their microstructure and properties. *Mater. Sci. Eng. A* **2020**, *772*, 138633. [[CrossRef](#)]
23. Lou, X.; Andresen, P.L.; Rebak, R.B. Oxide inclusions in laser additive manufactured stainless steel and their effects on impact toughness and stress corrosion cracking behavior. *J. Nucl. Mater.* **2018**, *499*, 182–190. [[CrossRef](#)]
24. Grasso, M.; Colosimo, B.M. Process defects and in situ monitoring methods in metal powder bed fusion: A review. *Meas. Sci. Technol.* **2017**, *28*, 0440051. [[CrossRef](#)]
25. Gordon, J.V.; Narra, S.P.; Cunningham, R.W.; Liu, H.; Chen, H.; Suter, R.M.; Beuth, J.L.; Rollett, A.D. Defect structure process maps for laser powder bed fusion additive manufacturing. *Addit. Manuf.* **2020**, *36*, 101552. [[CrossRef](#)]
26. Mukherjee, T.; DebRoy, T. Mitigation of lack of fusion defects in powder bed fusion additive manufacturing. *J. Manuf. Process.* **2018**, *36*, 442–449. [[CrossRef](#)]
27. Bayat, M.; Thanki, A.; Mohanty, S.; Witvrouw, A.; Yang, S.; Thorborg, J.; Tiedje, N.S.; Hattel, J.H. Keyhole-induced porosities in Laser-based Powder Bed Fusion (L-PBF) of Ti6Al4V: High-fidelity modelling and experimental validation. *Addit. Manuf.* **2019**, *30*, 100835. [[CrossRef](#)]
28. Mohr, G.; Johannsen, J.; Knoop, D.; Gärtner, E.; Hummert, K.; Emmelmann, C. Processing of a high-strength Al-Fe-Ni alloy using laser beam melting and its potential for in-situ graded mechanical properties. In Proceedings of the Lasers in Manufacturing Conference, Munich, Germany, 26–29 June 2017.
29. Xu, W.; Lui, E.W.; Pateras, A.; Qian, M.; Brandt, M. In situ tailoring microstructure in additively manufactured Ti-6Al-4V for superior mechanical performance. *Acta Mater.* **2017**, *125*, 390–400. [[CrossRef](#)]
30. Roehling, T.T.; Wu, S.S.Q.; Khairallah, S.A.; Roehling, J.D.; Soezeri, S.S.; Crumb, M.F.; Matthews, M.J. Modulating laser intensity profile ellipticity for microstructural control during metal additive manufacturing. *Acta Mater.* **2017**, *128*, 197–206. [[CrossRef](#)]
31. Shi, R.; Khairallah, S.A.; Roehling, T.T.; Heo, T.W.; McKeown, J.T.; Matthews, M.J. Microstructural control in metal laser powder bed fusion additive manufacturing using laser beam shaping strategy. *Acta Mater.* **2020**, *184*, 284–305. [[CrossRef](#)]
32. Kempen, K.; Vrancken, B.; Thijs, L.; Buls, S.; van Humbeeck, J.; Kruth, J.-P. Lowering thermal gradients in selective laser melting by pre-heating the baseplate. In Proceedings of the Solid Freeform Fabrication Symposium Proceedings, Austin, TX, USA, 12–14 August 2013.
33. Shiomi, M.; Osakada, K.; Nakamura, K.; Yamashita, T.; Abe, F. Residual stress within metallic model made by selective laser melting process. *CIRP Ann.* **2004**, *53*, 195–198. [[CrossRef](#)]
34. Williams, R.J.; Pigionio, A.; Rønneberg, T.; Jones, C.; Pham, M.-S.; Davies, C.M.; Hooper, P.A. In situ thermography for laser powder bed fusion: Effects of layer temperature on porosity, microstructure and mechanical properties. *Addit. Manuf.* **2019**, *30*, 100880. [[CrossRef](#)]
35. Mohr, G.; Nowakowski, S.; Altenburg, S.J.; Maierhofer, C.; Hilgenberg, K. Experimental determination of the emissivity of powder layers and bulk material in laser powder bed fusion using infrared thermography and thermocouples. *Metals* **2020**, *10*, 1546. [[CrossRef](#)]
36. Günter Briefs. *Nichtrostende Stähle—Teil 3: Technische Lieferbedingungen für Halbzeug, Stäbe, Walzdraht, Gezogenen Draht, Profile und Blankstahlerzeugnisse aus korrosionsbeständigen Stählen für allgemeine Verwendung*; DIN: Berlin, Germany, 2014.
37. Elisabeth Leistner. *Metallographic Instructions for Colour Etching by Immersion—Part III: Non-Ferrous Metals, Cemented Carbides and Ferrous Metals, Nickel-Base and Cobalt-Base Alloys*; D.V.S.-Verlag: Düsseldorf, Germany, 1998.
38. DIN EN ISO 643. *Mikrophotographische Bestimmung der Erkennbaren Korngröße*; DIN: Berlin, Germany, 2019.
39. Deng, P.; Yin, H.; Song, M.; Li, D.; Zheng, Y.; Prorok, B.C.; Lou, X. On the Thermal stability of dislocation cellular structures in additively manufactured austenitic stainless steels: Roles of heavy element segregation and stacking fault energy. *Jom* **2020**, *72*, 4232–4243. [[CrossRef](#)]
40. Heigel, J.C.; Lane, B.M. Measurement of the melt pool length during single scan tracks in a commercial laser powder bed fusion process. *J. Manuf. Sci. Eng.* **2018**, *140*, 051012–051017. [[CrossRef](#)]

41. Mohr, G.; Altenburg, S.J.; Ulbricht, A.; Heinrich, P.; Baum, D.; Maierhofer, C.; Hilgenberg, K. In-situ defect detection in laser powder bed fusion by using thermography and optical tomography—Comparison to computed tomography. *Metals* **2020**, *10*, 103. [[CrossRef](#)]
42. Vollmer, M.; Möllmann, K.-P. *Infrared Thermal Imaging: Fundamentals, Research and Applications*; John Wiley & Sons: Berlin, Germany, 2017.
43. Joachim, J. Untersuchung von Oxidationsprozessen an Oberflächen von FeCr-Legierungen und Austenitstahl Mittels Röntgenabsorptionsspektroskopie unter Streifendem Einfall. Ph.D. Thesis, Rheinische Friedrich-Wilhelms-Universität Bonn, Bonn, Germany, 2003.
44. Zhong, Y.; Liu, L.; Wikman, S.; Cui, D.; Shen, Z. Intragranular cellular segregation network structure strengthening 316L stainless steel prepared by selective laser melting. *J. Nucl. Mater.* **2016**, *470*, 170–178. [[CrossRef](#)]
45. Choo, H.; Sham, K.-L.; Bohling, J.; Ngo, A.; Xiao, X.; Ren, Y.; Depond, P.J.; Matthews, M.J.; Garlea, E. Effect of laser power on defect, texture, and microstructure of a laser powder bed fusion processed 316L stainless steel. *Mater. Des.* **2019**, *164*, 107534. [[CrossRef](#)]
46. Leicht, A.; Rashidi, M.; Klement, U.; Hryha, E. Effect of process parameters on the microstructure, tensile strength and productivity of 316L parts produced by laser powder bed fusion. *Mater. Charact.* **2020**, *159*, 110016. [[CrossRef](#)]
47. David, S.; Babu, S.; Vitek, J. Welding: Solidification and microstructure. *Jom* **2003**, *55*, 14–20. [[CrossRef](#)]
48. Stoudt, M.R.; Williams, M.E.; Levine, L.E.; Creuziger, A.; Young, S.A.; Heigel, J.C.; Lane, B.M.; Phan, T.Q. Location-specific microstructure characterization within IN625 additive manufacturing benchmark test artifacts. *Integr. Mater. Manuf. Innov.* **2020**, *9*, 54–69. [[CrossRef](#)]
49. Yadroitsev, I.; Krakhmalev, P.; Yadroitsava, I.; Johansson, S.; Smurov, I. Energy input effect on morphology and microstructure of selective laser melting single track from metallic powder. *J. Mater. Process. Technol.* **2013**, *213*, 606–613. [[CrossRef](#)]
50. Pazon, C.; Hryha, E.; Forêt, P.; Nyborg, L. Effect of argon and nitrogen atmospheres on the properties of stainless steel 316 L parts produced by laser-powder bed fusion. *Mater. Des.* **2019**, *179*, 107873. [[CrossRef](#)]
51. Dietrich, K.; Diller, J.; Dubiez-Le Goff, S.; Bauer, D.; Forêt, P.; Witt, G. The influence of oxygen on the chemical composition and mechanical properties of Ti-6Al-4V during laser powder bed fusion (L-PBF). *Addit. Manuf.* **2020**, *32*, 100980. [[CrossRef](#)]
52. Pazon, C.; Dietrich, K.; Forêt, P.; Hryha, E.; Witt, G. Mitigating oxygen pick-up during laser powder bed fusion of Ti-6Al-4V by limiting heat accumulation. *Mater. Lett.* **2021**, 129365. [[CrossRef](#)]
53. Pazon, C. The Process Atmosphere as a Parameter in the Laser-Powder Bed Fusion Process. Licentiate Thesis, Chalmers University of Technology, Göteborg, Sweden, 2019.
54. Kitchener, J.; Bockris, J.; Gleiser, M.; Evans, J. The solubility of oxygen in gamma iron. *Acta Metall.* **1953**, *1*, 93–101. [[CrossRef](#)]
55. Saeidi, K.; Gao, X.; Zhong, Y.; Shen, Z.J. Hardened austenite steel with columnar sub-grain structure formed by laser melting. *Mater. Sci. Eng. A* **2015**, *625*, 221–229. [[CrossRef](#)]
56. Bergmann, W. *Werkstofftechnik 1: Struktureller Aufbau von Werkstoffen-Metallische Werkstoffe-Polymerwerkstoffe-Nichtmetallisch-Anorganische Werkstoffe*; Carl Hanser Verlag GmbH Co. KG: Munich, Germany, 2013.
57. Krakhmalev, P.; Yadroitsava, I.; Fredriksson, G.; Yadroitsev, I. Microstructural and thermal stability of selective laser melted 316L stainless steel single tracks. *S. Afr. J. Ind. Eng.* **2017**, *28*. [[CrossRef](#)]
58. Bang, G.B.; Kim, W.R.; Kim, H.K.; Park, H.-K.; Kim, G.H.; Hyun, S.-K.; Kwon, O.; Kim, H.G. Effect of process parameters for selective laser melting with SUS316L on mechanical and microstructural properties with variation in chemical composition. *Mater. Des.* **2021**, *197*, 109221. [[CrossRef](#)]
59. Scipioni Bertoli, U.; Wolfer, A.J.; Matthews, M.J.; Delplanque, J.-P.R.; Schoenung, J.M. On the limitations of volumetric energy density as a design parameter for selective laser melting. *Mater. Des.* **2017**, *113*, 331–340. [[CrossRef](#)]
60. Prashanth, K.G.; Scudino, S.; Maity, T.; Das, J.; Eckert, J. Is the energy density a reliable parameter for materials synthesis by selective laser melting? *Mater. Res. Lett.* **2017**, *5*, 386–390. [[CrossRef](#)]